Label-free super-resolution stimulated Raman scattering imaging of biomedical specimens

JULIEN GUILBERT,[1] AWOKE NEGASH,[1] SIMON LABOUESSE[2], SYLVAIN GIGAN[1], ANNE SENTENAC[2], HILTON B. DE AGUIAR[1,*]

[1]*Laboratoire Kastler Brossel, ENS-Université PSL, CNRS, Sorbonne Université, Collège de France, 24 rue Lhomond, 75005 Paris, France*

[2]*Aix Marseille Univ, CNRS, Centrale Marseille, Institut Fresnel, Marseille, France*

[*]*h.aguiar@lkb.ens.fr*

Abstract: Far-field super-resolution microscopy has unravelled the molecular machinery of biological systems that tolerate fluorescence labelling. Conversely, stimulated Raman scattering (SRS) microscopy provides chemically selective high-speed imaging in a label-free manner by exploiting the intrinsic vibrational properties of specimens. Even though there were various proposals for enabling far-field super-resolution Raman microscopy, the demonstration of a technique compatible with imaging opaque biological specimens has been so far elusive. Here, we demonstrate a single-pixel-based, combined with robust structured illumination, that enables super-resolution in SRS microscopy. The methodology is straightforward to implement and provides label-free super-resolution imaging of thick specimens, therefore paving the way for probing complex biological systems when exogenous labelling is challenging.

1. Introduction

Far-field super-resolution imaging has emerged as a powerful tool in biology to unravel the details of the complex molecular machinery at play at the nanoscale. However, the great majority of super-resolution techniques are based on exogenous markers (fluorophores) that demand chemical preparation protocols and further studies to determine cell viability and specificity to a targeted molecule. Most importantly, fluorescence-based tools only report on the fluorophore information – dynamical or structural – leaving open many fundamental questions on the other outnumbering unlabelled molecular species: e.g., lipids and cholesterol molecular conformation and local composition [1–3] within lipid domains have remained undetected in real cells, or the local composition of the species forming membrane-less organelles which are currently unknown [4, 5]. Therefore, Raman microscopies have emerged as ideal tools for probing heterogeneous biological specimens [6], since they provide chemically resolved images using the intrinsic vibrational properties of molecules, that is, a label-free method. Yet, reaching fast super-resolution capabilities for opaque tissue imaging with Raman contrasts has remained challenging [7].

In the last decade, many attempts have been made to enable vibrational far-field super-resolution in SRS. Computational super-resolution methods, exploiting structured illumination microscopy (SIM), have been demonstrated for the spontaneous Raman contrast [8]. However, the usage of an imaging spectrometer is not compatible with thick tissues, as the resolution enhancement is only provided in one dimension, and the acquisition speeds are too slow for dynamic specimens. Very recently, a solution to this issue has been put forward, but the imaging methodology is still based on a wide-field geometry, potentially challenging to be applied in opaque specimens [9]. Alternatively, coherent Raman microscopies (CRM) could provide fast acquisition speeds: with the two most known contrast mechanisms being Coherent anti-Stokes Raman scattering (CARS) [10] and stimulated Raman scattering (SRS) [11–13]. However, there are various drawbacks that preclude biological specimens super-resolution imaging, in particular methods exploiting coherent control of vibrational dynamics [14–25]. Furthermore, in CARS, interference artifacts complicate chemical quantification analysis [26, 27]. In the case of the background-free

SRS process, the current mainstream is to exploit methods to control the dynamics of vibrational energy levels, however using unconventional power levels that may be phototoxic for biological specimens [20, 21, 23, 24, 28–31].

While combining computational super-resolution methods with SRS technology could overcome the above-mentioned issues, it cannot provide super-resolution capabilities in thick opaque tissues. Generally, the mathematical framework of computational methods is based on wide-field illumination which itself requires multi-pixel cameras. Unfortunately, wide-field cameras for SRS are technologically challenging because of SRS' unconventional detection scheme: SRS requires high-sensitivity radio-frequency lock-in amplifier (RF-LIA), which currently is only reliable in a single-pixel scheme. Despite recent developments of multi-pixel RF-LIA [32, 33], the pixel counts do not scale favorably for 1000's of pixels architecture needed in a camera. Furthermore, wide-field illumination is not suitable for thick tissue imaging due to the lack of sectioning capabilities: even if a camera did exist for using computational methods with SRS, it would be challenging to use due to aberrations and out-of-focus light generated by the solvent or the sample itself.

To address these challenges, we present a camera-less (aka single-pixel) chemically selective super-resolution imaging methodology compatible with opaque thick biological specimens. We are interested in demonstrating that this methodology indeed breaks the diffraction-limit resolution barrier of SRS microscopy. We start by describing the mathematical model used in the acquisition step, followed by a proof-of-principle aimed at demonstrating resolution beyond the theoretical diffraction limit. We then finalize demonstrating that its sensitivity is compatible with imaging biological specimens. Remarkably, the framework presented here has a simple alignment procedure: it is simpler than conventional SRS microscopy, which demands overlap of two tightly focused beams.

2. Concept

Specifically, we developed a single-pixel scheme (Fig. 1) compatible with computational super-resolution methods, therefore allowing for fast imaging capabilities exploiting SRS processes in the form of stimulated Raman gain (SRG) (Fig. 1a). In our arrangement, a structured stationary pump beam is shaped using a spatial light modulator (SLM) and is spatially and temporally overlapped with a focused Stokes beam that scans over the sample (using a set of galvanometric mirrors, Fig. 1b). After acquiring a series of SRS images with multiple structured illuminations (Fig. 1c) the data is treated with algorithms based on standard SIM mathematical framework to recover a super-resolved image [34, 35], as described below. We coin the method Single-pixel blind-SIM SRS (or blind-S^3 for short).

We describe the forward model of the acquisition procedure. In SRS, the signal detected (ΔI_S), a modulation transfer between the Pump and Stokes beams, at one pixel location (of the un-processed image) is given by [12]:

$$\Delta I_S \propto \Im\{\chi^{(3)}\} I_P I_S \tag{1}$$

where $\Im\{\chi^{(3)}\}$ is the imaginary part of the complex-valued nonlinear susceptibility of the sample (related to the Raman cross-section), I_P and I_S the intensity of the Pump and Stokes beam, respectively. In the case of the proposed acquisition method in blind-S^3, a static speckle pattern generated by the Pump beam spreads at the sample image plane where the Stokes beam is focused and scanned. To derive an image formation model, we assume a scalar approximation for the local intensity in one blind-S^3 image:

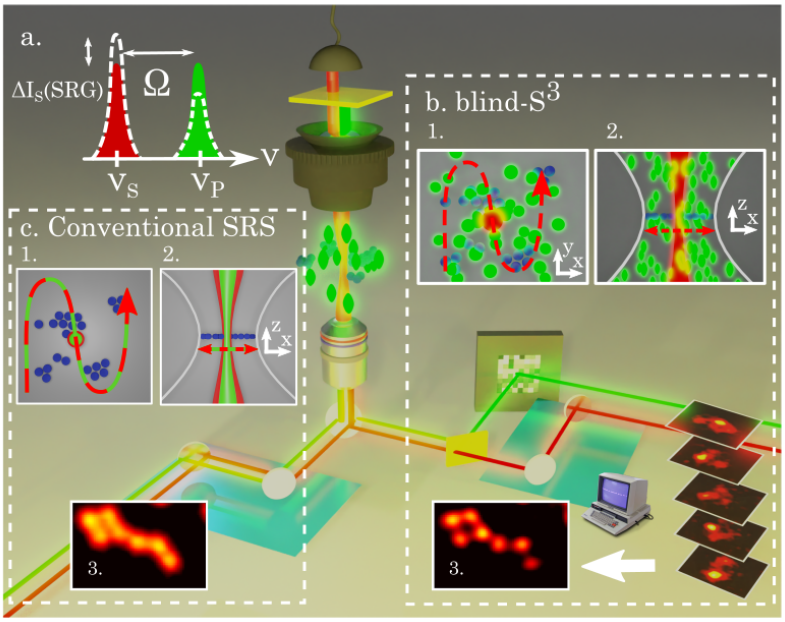

Fig. 1. Principle of blind-S^3. Schematic of the setup to achieve super resolution using the SRS process stimulated Raman Gain (SRG) (**a**) based on a single-pixel SIM scheme. Transverse (**b**1) and longitudinal (**b**2) planes of the scanning Stokes beam trajectory (red dash) over the stationary Raman-active specimen (blue) and structured Pump (green), in this case a speckle pattern. For every speckle realization, an SRS image is acquired forming an image stack that is passed to a SIM algorithm to reconstruct a super-resolved image (**b**3). (**c**) Conventional SRS, consisting in raster scanning co-propagating Pump and Stokes beams, is used as a control to demonstrate the increase in resolution when compared to standard imaging. Transverse (**c**1) and longitudinal (**c**2) planes of the Stokes and focused Pump beams (green and red dash) scanning trajectory over the stationary Raman-active specimen (blue).

$$\begin{aligned}\Delta I_S(x,y) &\propto \iint \Im\{\chi^{(3)}(x',y')\} I_P(x',y') I_S(x-x',y-y')\,dx'\,dy' \\ &\propto \left(\Im\{\chi^{(3)}\} I_P\right) \circledast I_S,\end{aligned} \tag{2}$$

An image acquired with blind-S^3 scheme obeys a forward model of the type $M_i = (O \times I_{SIM}) \circledast I_{Stokes}$, where M_i is an SRS image from a single speckle realization, O is the optical response of the excited object (more precisely, $\Im\{\chi^{(3)}\}$), I_{SIM} is the spatial distribution of the structured intensity at the Pump wavelength, I_{Stokes} is the effective PSF of the image formation system, and $\circledast$ denotes a convolution operation. This means that each single image acquired follow the standard forward models in computational super-resolution frameworks of incoherent processes. We chose to work with non-sinusoidal SIM patterns in order to be compatible with thick tissues: we use speckle patterns, since they are resilient in scattering specimens. While we tested the methodology with two SIM algorithms using no prior knowledge on the structured patterns I_{SIM} [34, 35], for the results presented we used the one described in Ref. [35]. In this approximation, we disregard coherent effects as SRS processes are inherently phase-matched.

3. Experimental

3.1. Microscope design and details

Briefly, the output power of a femtosecond laser source (Coherent, Chameleon Ultra Vision, 800 nm, 80 MHz repetition rate, 150 fs pulse length) pumps an optical parametric oscillator (APE, MIRA-OPO) that generates the Stokes beam, centered either at 1058 nm (Fig. 2, 3054 cm^{-1} Raman-shift) or 1042 nm (Fig. 4, 2903 cm^{-1} Raman-shift), and a small power fraction is used as the Pump beam. The Stokes beam is spectrally narrowed using a combination of grating (LightSmyth, T-1000-1040) and adjustable slit width for the purpose of increasing chemical selectivity. The Pump beam is also spectrally narrowed in a pulse-shaper setup using two gratings (LightSmyth Technologies, T-1400-800) and a digital micromirror device (DMD) placed in the Fourier plane (a description of the methods using DMDs for SRS spectroscopy can be found in Ref. [36]). The pump beam is amplitude-modulated at 1 MHz by an acousto-optic modulator (AA Opto-electronic, MT80-B30A1,5 VIS). The specimen is z-displaced using a piezo stage (Thorlabs, DRV517), and the signal generated by the sample is then collected by a 1.4 NA oil-immersion condenser, directed to a large-area detector (Thorlabs, DET100A2) and demodulated by a lock-in amplifier (Zurich Instruments, MFLI).

We used two configurations for SRS microscopy. Regardless of the configuration used, both beams are spatially and temporally combined at dichroic mirrors, whose location depends on the modality of SRS in use, and focused by an objective (Nikon, Plan APO IR, 60x, NA=1.27). To achieve the best compromise in terms of resolution enhancement (by having the Pump beam as a structured illumination) and sensitivity (by having the Stokes beam as the demodulated beam), we have designed a layout that allows us to quickly swap the direction of the Pump beam between the conventional SRS or blind-S^3 configurations using a combination of a half-wave waveplate and a polarizing beam splitter cube. For the blind-S^3 configuration, the Pump beam is sent onto a SLM (Meadowlark Optics, HSP512L-1300) to modulate the wavefront with a random phase. The SLM throughput is higher than 80% but it could be further enhanced by replacing the SLM by engineered diffusers since they have no absorption. Galvanometric mirror scanners are used to move either Pump and Stokes beams together (conventional) or Stokes only (blind-S^3). Typical average power measured before the objectives were 13 mW (conventional) and 41 mW (blind-S^3) for the Pump, and 25 mW for the Stokes beams. However, we note that the energy density levels used for blind-S^3 are inherently lower than the conventional SRS configuration: we have estimated a 5 times lower effective energy densities (i.e. product of the energy densities of the Pump and Stokes energy densities), taking into consideration the speckle envelope and the longer integration time in the blind-S^3 procedure, when compared to conventional method. Finally, after imaging in conventional SRS and blind-S^3, we image a large FOV to detect any sign of phototoxicity such as shown in the wide FOV images of the biological specimens.

3.2. Sample preparation

Samples presented in Fig. 2 were prepared by drop-casting the polystyrene beads on a coverslip and embedded in deuterated water to decrease the spectral congestion with the water vibrational response background. The various diameters (and standard deviation) used were: 239 nm (6 nm, PS Research Particles), 372 nm (10 nm, Polysciences, Inc.), 520 nm (16 nm, Thermo Scientific), 740 nm (22 nm, Thermo Scientific) and 990 nm (30 nm, Polysciences, Inc.). Mice brain slices were kindly provided by Laurent Bourdieu and experimental procedures were conducted in accordance with the institutional guidelines and in compliance with French and European laws and policies. All procedures were approved by the 'Charles Darwin' Ethics Committee (project number 26667). More precisely, 6-months old C57BL6 male mice were sacrificed, the extracted brain was then stored overnight in a solution of 4% paraformaldehyde and finally rinsed in phosphate buffer solution (PBS). Coronal slices of thickness 100 µm were then cut and stored in

PBS. Prior to experiments, the slices were placed between two cover slips with a 120-μm-thick spacer. HeLa cells (ATCC) were incubated with 400 μM oleic acid, washed, fixed with 4% paraformaldehyde, and stored at 4°C before imaging.

3.3. Resolution estimation

We assume that the theoretical transverse resolution results from the product of two focused Gaussian beams with two different wavelengths λ_p and λ_s for the Pump and Stokes wavelength respectively. Here, we use the Raman resonance 3054 cm^{-1} and the Rayleigh criteria to asses the resolution limit of each beam: $\Delta r_P = \frac{1.22\lambda_P}{2NA} = 384$ nm and $\Delta r_S = \frac{1.22\lambda_P}{2NA} = 508$ nm for the Pump and Stokes beam respectively where $NA = 1.27$, $\lambda_P = 800$ nm and $\lambda_S = 1058$ nm. Therefore, the theoretical resolution limit is $\Delta r_{SRS}^{conv} = \frac{1}{\sqrt{\frac{1}{\Delta r_P^2} + \frac{1}{\Delta r_S^2}}} = 307$ nm for conventional SRS while it is $\Delta r_{SRS}^{blind\,S^3} = \frac{\Delta r_{SRS}^{conv}}{\sqrt{2}} = 217$ nm for blind-S^3.

4. Results and discussion

4.1. Proof-of-concept of super-resolution capabilities beyond the diffraction limit

We first demonstrate the improvement in the transverse resolution, surpassing the diffraction-limit of usual SRS microscopy. In order to evaluate the gain in resolution, we compare blind-S^3 to the conventional scanning methods. For conventional SRS, the theoretical transverse resolution is $\Delta r^{Conv} = 307$ nm. This theoretical value is technically challenging to achieve with high numerical aperture (NA) objectives in the near-IR because the wavelengths of the two beams differ by hundreds of nanometers (spectral span necessary for fast quantification of lipids, proteins, and nucleic acids in SRS microscopy), in opposition to the visible range where diffraction limited performance has been reported [37]. Conversely, blind-S^3 transverse spatial resolution results from the doubling in resolution dictated by SIM and the speckle grain size limited by diffraction, leading to $\Delta r^{blind\,S^3} = 217$ nm. To show the superior transverse resolution in blind-S^3, we imaged 239 nm-diameter polystyrene beads with the two modalities (Fig. 2a-b). Clearly, conventional SRS (Fig. 2a) cannot resolve the beads transversely as the beads size is smaller than the theoretical resolution limit. After multiple speckle pattern illuminations, we feed the resulting images to a blind SIM algorithm to reconstruct a super-resolved image. Notably, blind-S^3 methodology (Fig. 2b) resolves several beads in the in-focus layer. The line profiles reveal the distance between the centers of the beads (242 nm) which matches well to the distance of close contact between two beads. We note that the effective region-of-interest (ROI) of blind-S^3 is modulated by the speckle envelope, hence decreasing the similarity of the two images in the edges of the beads cluster, yet not affecting the resolution gain (see below). The present findings show that the blind-S^3 methodology goes beyond the fundamental far-field diffraction-limit resolution of SRS microscopy, by improving the resolution $\geq \sqrt{2}$, without addition of exogenous signal enhancers and using excitation energy densities lower than conventional SRS microscopy, therefore decreasing probability of nonlinear phototoxic effects.

Remarkably, super-resolution in blind-S^3 comes with intrinsic high z-sectioning capabilities. In each illumination during the blind-S^3 procedure, an image is formed based on a wide-field geometry model, that is, an object is convoluted with a linear point-spread function (PSF). In a hypothetical conventional wide-field SRS microscope using multi-pixel cameras, the excitation beams would overlap a large volume. This would in turn reduce the sensitivity due out-of-focus shot-noise, therefore deteriorating image quality and resolution due to the background noise (shot-noise). Conversely, the blind-S^3 methodology improves sectioning, without resorting to cameras, as the nonlinear optical response is local in the longitudinal direction: because SRS signals are only generated within the overlap region of the two beams, each SRS image does not contain appreciable out-of-focus shot-noise. To demonstrate the sectioning capabilities of

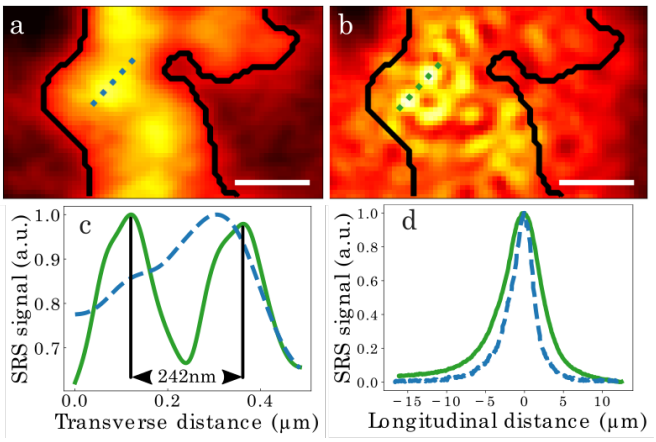

Fig. 2. Proof-of-concept of blind-S^3 capabilities to image beyond the diffraction-limit. Conventional (**a**) and blind-S^3 (**b**) images of 239 nm-diameter polystyrene beads, and line profiles (**c**) showing the increase in transverse resolution of blind-S^3 (line) compared to conventional methods (dash). (**d**) Conventional SRS (dash) and blind-S^3 (line) sectioning capabilities characterization. All scale bars: 500 nm. Pixel dwell times are 73 μs and 300 μs for conventional and blind-S^3 methods, respectively.

blind-S^3, we probed a thin film of oil (of few μm) by scanning it in the longitudinal direction. Note that we collect the signal generated for each z-position on a ≈10 mm-wide detector, hence, not in a confocal geometry. Clearly, conventional SRS and blind-S^3 give a peaked response which means that those two techniques have inherent longitudinal sectioning (Fig. 2d). Indeed, the conventional SRS microscope is able to show such z-sectioning capability, due to its nonlinear longitudinal PSF.

Contrary to conventional methods in super-resolution microscopy, in blind-S^3 it is not straightforward to compare the reconstructed images with a "ground truth" object. This arises from the fact that the FOV in blind-S^3 is modulated by the speckle envelope, which is smaller than conventional SRS microscopy. Therefore, we devised another methodology to insure if the reconstruction was indeed reaching super-resolution capabilities. We imaged commercially available calibrated polystyrene beads of various sizes, which are well-known to aggregate and form close-packed structures. Therefore, we can use the bead close contact distance as a proxy for the bead diameter. We measured the close contact distances of several beads for several sizes ranging from smaller than to several times the resolution limit, and also for two different objectives with different NAs. Although the method is somewhat subjective, we were careful to chose "spot centers" that had the smallest distances possible. Following this procedure, we noticed that maximum spot-to-spot center were indeed limited by the bead size, that is, in the 360 nm bead diameter we did not see 240 nm spatial fluctuations. The outcome of this procedure is shown Fig. 3 and the agreement between the nominal bead diameter and the retrieved diameter therefore confirms that the features observed in the blind-S^3 reconstructions indeed correspond to physical features beyond the diffraction limit.

4.2. Biological compatibility

To demonstrate blind-S^3 compatibility with biological specimens, we image standard cell lines and mouse brain tissues. Conventional SRS reveals several μm-large droplets within the cell in the FOV (Fig. 4a). Close-up images show different cluster morphology (Fig. 4b), and increased resolution gain with blind-S^3 from the line profiles of selected ROI (Fig. 4c). To demonstrate

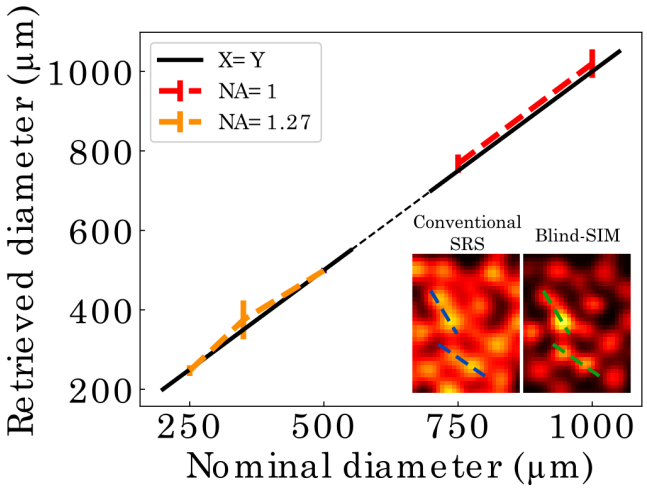

Fig. 3. Transverse resolution analysis for blind-S^3. Outcome analysis of the images of various close-contact beads pairs: We use close-contact distances as a proxy for the bead diameter. The inset shows representative images used for analysis, with the dashed lines representing some of the beads chosen for evaluation.

capabilities for aberrant and opaque tissues, we have further imaged highly scattering brain slices at 8 μm-deep in the sample (Fig. 4d-e) with line profiles demonstrating increased resolution power of the myelin structures (Fig. 4f). The close-up images with super-resolution capabilities (Fig. 4e) reveal that the structure of the myelin in the tissue is actually not as symmetrically perfect as inferred from the low-resolution images. These results show that the method is compatible with thick tissue imaging, despite being completely opaque, a situation where using a hypothetical SRS widefield camera approach may fail due to background shot-noise.

We consider the effects of the idle speckle upon illumination of the sample. One potential hazardous effect is due heating. While the Stokes is point scanning, there are other regions of the speckle pattern that constantly illuminate the sample therefore potentially presenting a phototoxic effect. Here, we assume the peak power of the speckle is too weak to induce nonlinear photodamage (at least not observed in our experiments and shown by the large FOV images after the acquisition procedure), and we consider what is the temperature rise due to the small, but non-negligible, absorption of water at the pump wavelength. This is a safe assumption as the speckle power used in the experiments is spread over a region that is over 10× larger that the spot size of the conventional SRS imaging system: this would represent a 100× weaker peak power. To analyze the heat effects, we use a well-established heat propagation framework used in the context of optogenetics [38] which have shown to be accurate in previous experiments. The simulation was performed with a speckle illumination power of 1 W (20× higher than the experiments) and envelope size of 10 μm. Since heat-diffusion is faster than the image acquisition, the speckle grains are washed out and only the speckle envelope is important to be considered. Hence, we plot the maximum of this thermal envelope in Fig. 5 for a illumination that stopped at 10 s and a continuous one. One can see that the steady-state value saturates at 0.023 K W^{-1}MHz^{-1}, which corresponds to temperature rise < 0.1 K in our experiments. Note that the recently reported photothermal SRS signal [39] could be present, and therefore have a higher temperature rise than due to the Pump speckle itself. However, in the simulations above, we consider the Pump speckle envelope, which does not go through the thermal SRS effect as a whole. Furthermore, this thermal SRS heat mechanism would be highly local and quickly dissipated as the overlap of

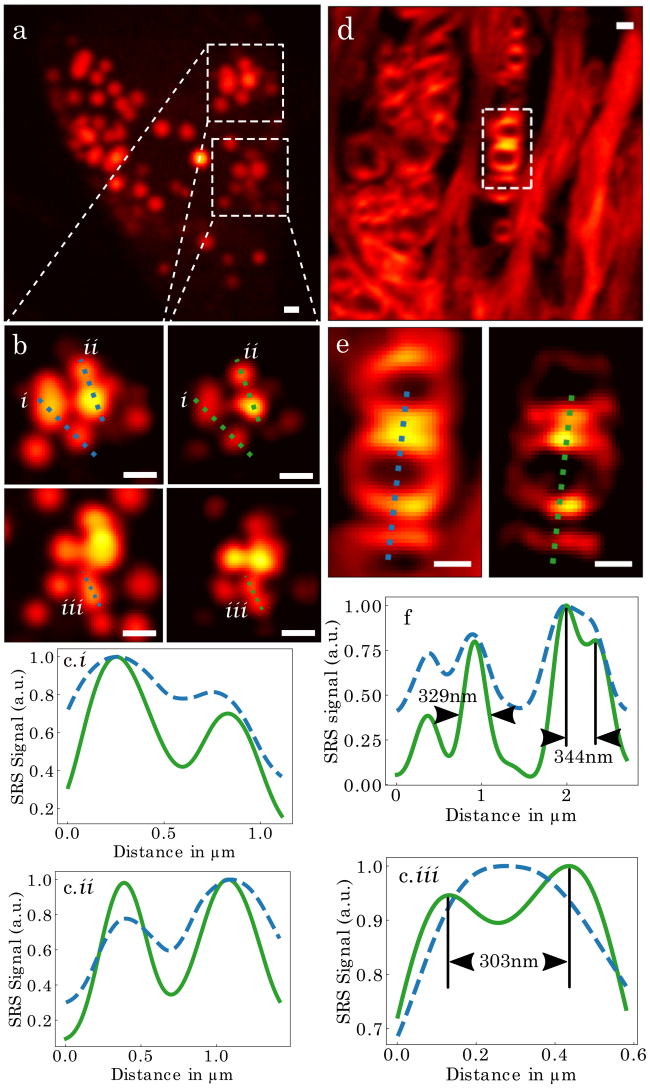

Fig. 4. Bio-compatibility capabilities of blind-S^3 at reduced excitation energy densities. (**a**) Large FOV imaging of lipid droplets within HeLa cells (conventional SRS). Two zoomed-in ROIs (**b**) are depicted by dashed boxes with conventional SRS (left panels) and blind-S^3 (right panels) methods, with various line profiles shown (c, **i, ii** and **iii**) for conventional SRS (dash) and blind-S^3 (line). (**d**) Large FOV image of opaque 100 µm thick mouse cerebellum (conventional SRS). A zoomed-in ROI (**e**) is depicted by dashed boxes with conventional SRS (left panel) and blind-S^3 (right panel) methods, with a line profile chosen (**f**) for conventional (dash) and blind-S^3 (line) methods. All scale bars: 500 nm. Pixel dwell times are top row (bottom row), 90 μs and 180 μs (100 μs and 270 μs) for conventional and blind-S^3 methods, respectively, in panel **b**., and 100 μs and 300 μs for conventional and blind-S^3 methods, respectively, in panel **e**.

the Pump and Stokes beams is small and as we use water (fast thermal dissipation). Finally, to reduce the temperature rise due to the idle speckle illuminating the sample, one could alleviate this by conjugating the excitation speckle plane with a scanning mirror (for instance, using a

digital micromirror device).

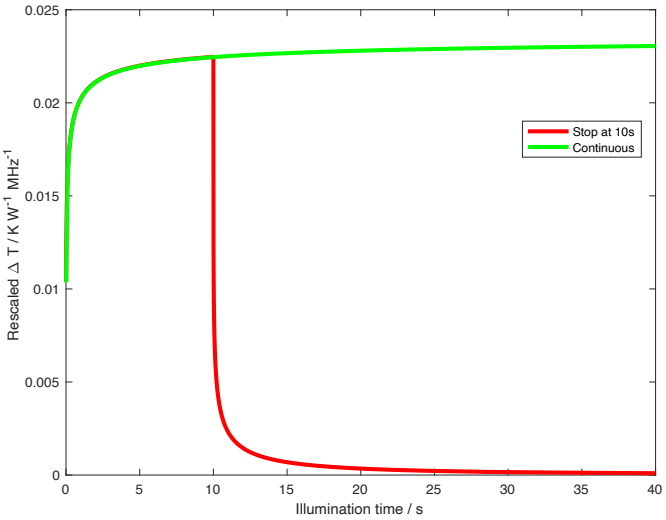

Fig. 5. Maximum temperature rise of the speckle evelope.

4.3. Discussion

Here, we have demonstrated above that the proposed method reaches resolution beyond the diffraction limit. We further demonstrated that the low excitation power used ensures low phototoxicity. Nevertheless, we discuss below potential issues in the methodology and how to overcome them with further engineering.

Further technical improvements could greatly overcome current limitations in these proof-of-principle experiments. In regards to speed and/or increasing the FOV, the current implementation used classical frequency-domain spectral narrowing methods which have lower throughput therefore limiting the largest FOV available (i.e. larger FOV requires more laser power to keep the energy density constant). To address this issue, we envision an improvement using spectral focusing methods, therefore increasing the FOV of the measurement as it can use all laser power available. Despite these proposed follow-up improvements, the blind-S^3 technique is able to super-resolve in strongly opaque biological tissues: indeed, in biomedical applications, aberrations deteriorate the PSF of the microscope, perhaps explaining the lower resolution attained in the biological specimens observed here. Here, while the penetration depth of brain tissues was limited to 8μm, with recent advances of deep SRS imaging [40], this penetration depth could in principle be extended. Finally, we speculate that blind-S^3 could be a route to reach far-field nanoscopy (sub-100-nm resolution). A straightforward route for nanoscopy is to decrease the excitation wavelengths in the UV [37]. However, UV radiation are known to enhance phototoxicity (for instance, by generating DNA photoradicals [41]). With blind-S^3, one could still use excitation lasers in the visible range, and reach resolutions below the 100-nm barrier because of the structured illumination approach.

5. Conclusions

In conclusion, we have designed and demonstrated a single-pixel super-resolution technique that is straightforward to implement, i.e. simpler than a conventional SRS microscope. We demonstrated that this technique can image beyond the diffraction limit ($\sqrt{2}$), and that it did

not show phototoxic effects in biological specimens imaged. blind-S^3 is an universal approach in the sense that it depends neither on the specific vibrational mode ultrafast dynamics [29], nor it requires vibrational signal enhancers [42, 43], or *a priori* knowledge about the specimen, for instance, as gained in the training of neural networks methods [44, 45]. Therefore, these achievements have overcome a decade-long challenge in SRS imaging, paving the way for investigating matter in its most natural environments.

After the initial submission of the current work [46], an alternative computational approach has been experimentally demonstrated for SRS super-resolution of biological specimens [47] using deconvolution methods.

6. Acknowledgements

We thank Claudio Moretti, Nabil Garroum, Arnaud Leclercq and Quentin Anty for technical support on the microscope development, Bernhard Rauer for fruitful discussions, Abdou Rachid Thiam and Mohyeddine Omrane for providing the HeLa cells, Laurent Bourdieu for providing the brain slices, and Pascal Berto and Benoît C. Forget for discussion on the heating effects and its simulation. This research has been funded by the LabEX ENS-ICFP (ANR-10-LABX-0010/ANR-10-IDEX-0001-02 PSL*), H2020 FETOPEN project "Dynamic" (EC-GA-863203), European Research Council ERC Consolidator Grant (SMARTIES - 724473). S.G. is a member of the Institut Universitaire de France.

References

1. E. Sezgin, I. Levental, S. Mayor, and C. Eggeling, "The mystery of membrane organization: composition, regulation and roles of lipid rafts," Nat. Rev. Mol. Cell Biol. **18**, 361–374 (2017).
2. J. Ando, M. Kinoshita, J. Cui, *et al.*, "Sphingomyelin distribution in lipid rafts of artificial monolayer membranes visualized by Raman microscopy," Proc. Natl. Acad. Sci. U. S. A. **112**, 4558–4563 (2015).
3. S. H. Donaldson and H. B. De Aguiar, "Molecular Imaging of Cholesterol and Lipid Distributions in Model Membranes," J. Phys. Chem. Lett. **9**, 1528–1533 (2018).
4. Y. Shin and C. P. Brangwynne, "Liquid phase condensation in cell physiology and disease." Sci. (New York, N.Y.) **357**, eaaf4382 (2017).
5. A. C. Murthy, G. L. Dignon, Y. Kan, *et al.*, "Molecular interactions underlying liquid-liquid phase separation of the FUS low-complexity domain," Nat. Struct. Mol. Biol. **26**, 637–648 (2019).
6. J.-X. Cheng and X. S. Xie, "Vibrational spectroscopic imaging of living systems: An emerging platform for biology and medicine," Science **350**, aaa8870–aaa8870 (2015).
7. K. Fujita, *Label-free super-resolution microscopy* (2019).
8. K. Watanabe, A. F. Palonpon, N. I. Smith, *et al.*, "Structured line illumination raman microscopy," Nat Commun **6**, 10095 (2015).
9. C. Hu, Z. Jiang, P. Liu, *et al.*, "Super-resolved Raman imaging via galvo-painted structured line illumination," Opt. Lett. **47**, 5949–5952 (2022). Publisher: Optica Publishing Group.
10. A. Zumbusch, G. R. Holtom, and X. S. Xie, "Three-dimensional vibrational imaging by coherent anti-stokes raman scattering," Phys. Rev. Lett. **82**, 4142–4145 (1999).
11. C. W. Freudiger, W. Min, B. G. Saar, *et al.*, "Label-free biomedical imaging with high sensitivity by stimulated raman scattering microscopy," Science **322**, 1857–1861 (2008).
12. P. Nandakumar, A. Kovalev, and A. Volkmer, "Vibrational imaging based on stimulated Raman scattering microscopy," New journal physics **11**, 33026 (2009).
13. E. Ploetz, S. Laimgruber, S. Berner, *et al.*, "Femtosecond stimulated Raman microscopy," Appl. Phys. B **87**, 389–393 (2007).
14. W. P. Beeker, P. Groß, C. J. Lee, *et al.*, "A route to sub-diffraction-limited CARS microscopy," Opt. Express **17**, 22632 (2009).
15. W. P. Beeker, C. J. Lee, K.-J. Boller, *et al.*, "Spatially dependent rabi oscillations: An approach to sub-diffraction-limited coherent anti-stokes raman-scattering microscopy," Phys. Rev. A **81**, 012507 (2010).
16. W. Liu and H. Niu, "Diffraction barrier breakthrough in coherent anti-stokes raman scattering microscopy by additional probe-beam-induced phonon depletion," Phys. Rev. A **83**, 023830 (2011).
17. C. Cleff, P. Groß, C. Fallnich, *et al.*, "Ground-state depletion for subdiffraction-limited spatial resolution in coherent anti-stokes raman scattering microscopy," Phys. Rev. A **86**, 023825 (2012).
18. L. Gong and H. Wang, "Breaking the diffraction limit by saturation in stimulated-raman-scattering microscopy: A theoretical study," Phys. Rev. A **90**, 013818 (2014).
19. Y. Yonemaru, A. F. Palonpon, S. Kawano, *et al.*, "Super-spatial- and -spectral-resolution in vibrational imaging via saturated coherent anti-stokes raman scattering," Phys. Rev. Appl. **4**, 014010 (2015).

20. W. R. Silva, C. T. Graefe, and R. R. Frontiera, "Toward label-free super-resolution microscopy," ACS Photonics **3**, 79–86 (2016).
21. D. Kim, D. S. Choi, J. Kwon, *et al.*, "Selective suppression of stimulated raman scattering with another competing stimulated raman scattering," J. Phys. Chem. Lett. **8**, 6118–6123 (2017).
22. D. S. Choi, B. J. Rao, D. Kim, *et al.*, "Selective suppression of CARS signal with three-beam competing stimulated raman scattering processes," Phys. Chem. Chem. Phys. **20**, 17156–17170 (2018).
23. B. J. Rao, D. S. Choi, and M. Cho, "Selective suppression of CARS signal with two competing stimulated raman scattering processes," The J. Chem. Phys. **149**, 234202 (2018).
24. C. T. Graefe, D. Punihaole, C. M. Harris, *et al.*, "Far-field super-resolution vibrational spectroscopy," Anal. Chem. **91**, 8723–8731 (2019).
25. S. Lim, D. S. Choi, H. Rhee, and M. Cho, "An efficient switching-off of coherent anti-stokes raman scattering via double stimulated raman scattering processes of heteromolecular vibrational modes," The J. Phys. Chem. B **124**, 3583–3590 (2020).
26. G. Wurpel and M. Muller, "Water confined by lipid bilayers: A multiplex CARS study," Chem. Phys. Lett. **425**, 336–341 (2006).
27. C. H. Camp Jr, Y. J. Lee, J. M. Heddleston, *et al.*, "High-Speed Coherent Raman Fingerprint Imaging of Biological Tissues," Nat. Photonics **8**, 627 (2014).
28. L. Gong and H. Wang, "Suppression of stimulated raman scattering by an electromagnetically-induced-transparency–like scheme and its application for super-resolution microscopy," Phys. Rev. A **92**, 023828 (2015).
29. R. C. Prince, R. R. Frontiera, and E. O. Potma, "Stimulated raman scattering: From bulk to nano," Chem. Rev. **117**, 5070–5094 (2018).
30. L. Gong, W. Zheng, Y. Ma, and Z. Huang, "Saturated stimulated-raman-scattering microscopy for far-field superresolution vibrational imaging," Phys. Rev. Appl. **11**, 034041 (2019).
31. T. Würthwein, N. Irwin, and C. Fallnich, "Saturated raman scattering for sub-diffraction-limited imaging," The J. Chem. Phys. **151**, 194201 (2019).
32. C.-S. Liao, P. Wang, P. Wang, *et al.*, "Spectrometer-free vibrational imaging by retrieving stimulated Raman signal from highly scattered photons," Sci. Adv. **1** (2015).
33. A. Ragni, G. Sciortino, M. Sampietro, *et al.*, "Multi-channel lock-in based differential front-end for broadband Raman spectroscopy," Integration **67**, 44–49 (2019).
34. E. Mudry, K. Belkebir, J. Girard, *et al.*, "Structured illumination microscopy using unknown speckle patterns," Nat. Photonics **6**, 312–315 (2012).
35. L.-H. Yeh, L. Tian, and L. Waller, "Structured illumination microscopy with unknown patterns and a statistical prior," Biomed. Opt. Express **8**, 695 (2017).
36. P. Berto, C. Scotté, F. Galland, *et al.*, "Programmable single-pixel-based broadband stimulated raman scattering," Opt. Lett. **42**, 1696 (2017).
37. Y. Bi, C. Yang, Y. Chen, *et al.*, "Near-resonance enhanced label-free stimulated raman scattering microscopy with spatial resolution near 130 nm," Light Sci Appl **7**, 81 (2018).
38. A. Picot, S. Dominguez, C. Liu, *et al.*, "Temperature Rise under Two-Photon Optogenetic Brain Stimulation," Cell Reports **24**, 1243–1253.e5 (2018). Publisher: Cell Press.
39. Y. Zhu, X. Ge, H. Ni, *et al.*, "Stimulated Raman photothermal microscopy toward ultrasensitive chemical imaging," Sci. Adv. (2023). Publisher: American Association for the Advancement of Science.
40. L. Gong, S. Lin, and Z. Huang, "Stimulated Raman Scattering Tomography Enables Label-Free Volumetric Deep Tissue Imaging," Laser & Photonics Rev. p. 2100069 (2021).
41. J.-Y. Liang, J.-M. P. Yuann, C.-W. Cheng, *et al.*, "Blue light induced free radicals from riboflavin on e. coli dna damage," J. Photochem. Photobiol. B: Biol. **119**, 60–64 (2013).
42. L. Gong, W. Zheng, Y. Ma, and Z. Huang, "Saturated Stimulated-Raman-Scattering Microscopy for Far-Field Superresolution Vibrational Imaging," Phys. Rev. Appl. **11**, 034041 (2019).
43. H. Xiong, N. Qian, Y. Miao, *et al.*, "Super-resolution vibrational microscopy by stimulated Raman excited fluorescence," Light. Sci. & Appl. **10**, 87 (2021).
44. H. Lin, H. J. Lee, N. Tague, *et al.*, "Microsecond fingerprint stimulated Raman spectroscopic imaging by ultrafast tuning and spatial-spectral learning," Nat. Commun. **12**, 3052 (2021).
45. C. M. Valensise, A. Giuseppi, F. Vernuccio, *et al.*, "Removing non-resonant background from CARS spectra via deep learning," APL Photonics **5**, 061305 (2020).
46. J. Guilbert, A. Negash, S. Labouesse, *et al.*, "Label-free super-resolution chemical imaging of biomedical specimens," bioRxiv p. 2021.05.14.444185 (2021). Publisher: Cold Spring Harbor Laboratory.
47. H. Jang, Y. Li, A. A. Fung, *et al.*, "Super-resolution SRS microscopy with A-PoD," Nat. Methods **20**, 448–458 (2023). Number: 3 Publisher: Nature Publishing Group.